

Recent Advances in Ligand-Free, Charged and Defect-Rich Catalysts Developed by Laser Ablation and Processing in Liquids

Authors: Dongshi Zhang, Jun Liu,, Pengfei Li, Zhenfei Tian, Changhao Liang, Changhao Liang

Date: 2017-10-31T00:00:00+00:00

Abstract

Catalysts are the foundation of sustainable and renewable energies to address the depletion of natural fossil fuels problem. Because the catalysts' activity is surface chemistry dependent, those "naked", so-called ligand-free catalysts with more active sites exposing to the reactants are more preferable. With ligand-free, highly surface charged nanomaterials as the innate products, a newly emerging technique laser synthesis and processing in liquids is gaining increasing attention. The priority of laser-synthesized ligand-free metallic catalysts over chemically-synthesized counterparts has been confirmed by increasing groups through comparative studies on their catalytic activities. Besides the ligand-free metallic catalysts, this technique also excels at synthesis of bimetallic-alloy, core-shell and defect-rich semiconductor catalysts, and show good compatibility with other techniques (e.g., hydrothermal treatment and electrophoresis) to develop advanced catalysts such as ternary oxide, doped semiconductor, supported composite, nanoparticle-polymer matrix and film catalysts. Following the concept of why to choose, how to synthesize and where to use, in this review, we first introduce the advantages of this technique and the synthesized catalysts, secondly show how to develop complex catalysts using the laser-generated particles as the building blocks, and finally present the exciting application examples for photodegradation, water splitting and fuel cells.

Full Text

Recent Advances in Ligand-Free, Charged and Defect-Rich Catalysts Developed by Laser Ablation and Processing in Liquids

Dongshi Zhang, Jun Liu, Pengfei Li, Zhenfei Tian, Changhao Liang*

Key Laboratory of Materials Physics, Anhui Key Laboratory of Nanomaterials and Nanotechnology, Institute of Solid State Physics, Hefei Institutes of Physical Science, Chinese Academy of Sciences, Hefei 230031, China

E-mail: chliang@issp.ac.cn, dongshi17@126.com

Keywords: Ligand-free; Laser ablation in liquids; Laser processing in liquids; Catalysis; Doping

Abstract

Catalysts are fundamental to sustainable and renewable energy solutions addressing the depletion of natural fossil fuels. Since catalytic activity is surface chemistry-dependent, “naked” or ligand-free catalysts with more exposed active sites are highly desirable. Laser synthesis and processing in liquids (LSPL) is an emerging technique that inherently produces ligand-free, highly surface-charged nanomaterials, garnering increasing attention. Comparative studies by numerous groups have confirmed the superiority of laser-synthesized ligand-free metallic catalysts over chemically-synthesized counterparts in catalytic activity. Beyond metallic catalysts, this technique excels at synthesizing bimetallic alloys, core-shell structures, and defect-rich semiconductor catalysts. It also demonstrates excellent compatibility with other methods (e.g., hydrothermal treatment and electrophoresis) for developing advanced catalysts such as ternary oxides, doped semiconductors, supported composites, nanoparticle-polymer matrices, and film catalysts. Following the conceptual framework of why to choose, how to synthesize, and where to use, this review first introduces the advantages of this technique and its synthesized catalysts. We then demonstrate how to develop complex catalysts using laser-generated particles as building blocks, and finally present exciting application examples in photodegradation, water splitting, and fuel cells.

Introduction

Catalysis has become a research hotspot in both academia and industry due to its widespread applications in developing sustainable/renewable energies to mitigate the global energy crisis and in photodegrading toxic organic molecules to reduce environmental contamination [?]. To meet these demands, both physical top-down and chemical bottom-up methods have been extensively exploited to synthesize nanoscale catalysts with well-controlled size, morphology, and extraordinary activity [?]. However, ligand-involved wet-chemical approaches require capping agents that adversely affect catalyst performance [?], making ligand removal through thermal or oxidative treatment inevitable. This removal process can alter the chemical and physical properties of the treated catalysts. Ligands conjugated on catalyst surfaces can block active sites and cause catalyst deactivation [?]. After two decades of development, an interdisciplinary technique involving laser ablation of bulk targets in liquids (LAL) and laser processing of colloids in liquids (LPL) has emerged as a facile and efficient one-step

tool for nanomaterial synthesis, particularly producing ligand-free nanoparticles (NPs) that are highly appealing for catalytic applications.

LAL is a top-down technique that employs pulsed lasers to ablate targets immersed in liquids (e.g., water [?], ionic liquid [?], organic solvent [?], surfactant [?], or polymer-containing solution [?] or their mixtures [?]). During LAL, a plasma with high temperature (3000–7000 K) and high pressure ($1.3 \times 10 - 5.7 \times 10$ Pa) is generated initially [?], causing atomization and ionization of the ablated material and its ejection into the liquid, leaving behind ablated grooves [?]. During rapid plasma quenching, energy is transferred to the surrounding liquid and simultaneously a cavitation bubble forms, capturing most of the colloids inside [?]. The fast plasma generation-quenching process ($10^{-1} - 10^{-1}$ s) facilitates the production and preservation of rich defects in the nucleated nanomaterial catalysts [?]. After bubble collapse, the colloids are released into the liquid and undergo particle coalescence [?, ?], attachment [?, ?], or self-assembly [?] to evolve into various nanomaterials, including metallic, oxide, carbide, nitride, and nanoparticle-polymer composites [?, ?]. Because LAL synthesis is completely different from “mild” chemical methods, novel nanomaterials with unique physical and chemical properties are anticipated, and published literature has confirmed this speculation (see Section 2). In particular, the innate ligand-free nanomaterials generated by LAL are attractive for catalytic applications because they free researchers from complicated cleaning procedures for ligand removal (including centrifugation, solvent extraction, calcination, or ozonolysis) and provide “naked” bare surfaces with high activity, eliminating ligand blocking effects.

LPL includes fragmentation in liquids (LFL) and laser melting in liquids (LML). LFL operates through photothermal vaporization [?] or Coulomb explosion mechanisms [?], while LML relies on laser-induced heating [?]. LPL is often used to narrow size distribution [?], introduce surface defects [?], purify NP phases [?], or fuse colloidal mixtures into alloy particles [?] and metal-encapsulated oxide composites [?]. LAL-synthesized colloids [?, ?], chemically-synthesized NPs [?], and microscale powders [?, ?] are all suitable for LPL, ensuring its widespread applicability for tailoring catalyst physical and chemical properties.

Fundamental research on LAL and LPL has progressed rapidly over the past two decades [?, ?, ?], and LAL/LPL-synthesized colloids show high compatibility with other methods, enabling further construction of ternary-oxide, doped, supported, nanoparticle-polymer, and film catalysts (Section 3). Driven by the great demand for renewable and sustainable energies, the use of LAL/LPL-synthesized NPs for catalytic applications has advanced steadily with new results emerging continuously. This review examines the development of LAL/LPL-synthesized catalysts from a methodological perspective, revealing advantages originating from catalyst diversity (e.g., alloy, core-shell, hollow, composite), ligand-free surface chemistry, surface charge, unsaturated coordination, and oxygen vacancy introduction. We also discuss how to use LAL/LPL-synthesized nanoparticles as building blocks to construct ternary

oxide, doped semiconductor, supported composite, nanoparticle-polymer, and film catalysts, highlighting their integration capabilities for advanced catalysts and electrodes. Finally, representative literature demonstrating distinguishable features of LAL/LPL-synthesized nanomaterials for catalytic applications (photodegradation, water splitting, direct methanol fuel cells, and electrochemical detection) is introduced (Section 4), followed by perspectives on current challenges and future trends (Section 5).

[Figure 1: see original paper] Schematic of LAL and LPL processes and the obtainable bimetallic-alloy (core-shell, intermetallic and heterostructure) and oxide (e.g., Ge-doped γ -Fe₂O₃, anatase and rutile TiO₂, ZnSnO) catalysts and the typical shapes of synthesized catalysts.

Advantages of LSPC for Catalysis

Catalyst Diversity by LAL

2.1.1 Bimetallic Catalysts Bimetallic nanoparticles, classified into three types including core-shell, intermetallic/alloyed structures, and heterostructures, often outperform their monometallic counterparts as catalysts due to synergistic effects between the metals [?]. However, synthesizing bimetallic NPs, especially alloyed NPs, is very complicated and difficult [?], which indirectly increases production costs and hinders extensive practical use. LAL and LPL techniques conveniently transform bulk bimetallic targets (commercial [?, ?] or self-pressed pellets using powder mixtures [?]) and colloidal mixtures [?, ?] into different kinds of bimetallic nanoparticles (Figure 2a [Figure 2: see original paper]), such as core-shell (e.g., Fe@Au [?], Cu@Ag [?]), heterostructure (e.g., Cu-Ag [?]), and alloys (e.g., AgAu [?, ?], PtCo [?], PtFe [?], PtNi [?]). With enriched diversity in LAL-synthesized alloy NPs, many tests have evaluated their activities for various catalytic reactions. In 2014, Ma and coworkers confirmed a strong synergistic effect between Au and Pt during 4-nitrophenol reduction, while no synergistic effect was found using mixed Au and Pt NPs (Figure 2b) [?]. Later, Oko et al. showed that Au Pt alloy NPs derived from LAL could significantly enhance the oxidation current of ascorbic acid by three times compared to Au NPs [?]. Recently, Barcikowski's group alloyed Ni with Mo into NiMo alloy NPs by LAL and demonstrated their synergistic effect for oxygen evolution reaction (OER) (Figure 2c) [?]. Surprisingly, LAL-synthesized Cu Ni alloy nanoparticles outperform Cu, Ni, and even Pt NPs as cocatalysts with TiO₂ nanorods for photocatalytic H₂ evolution (Figure 2d) [?]. These reports reveal the competence of LAL in producing alloy NPs. Considering the cost-effective nature of LAL, which requires only inexpensive bulk targets and liquids, a new avenue for developing various bimetallic NPs is being paved.

[Figure 2: see original paper] Bimetallic nanoparticles synthesized by LAL and their catalytic performance. (a) Core-shell, intermetallic and heterostructure Ag-Cu NPs with different Cu atom ratios as determined by high-angle annular

dark field (HAADF), energy dispersive X-ray (EDX) mapping and line scan. Adapted with permission from Ref [?]. Copyright 2014 American Chemical Society. (b) Variation of the normalized k_{app} with respect to the Pt content in Pt Au alloy-NP/CeO -NTs. Adapted with permission from Ref [?]. Copyright 2014 Royal Society of Chemistry. (c) Comparison of the OER activity of Mo, Ni and Ni Mo alloy colloid as well as a 40:60 mixture of nickel with molybdenum colloid. Adapted with permission from Ref [?]. Copyright 2016 Elsevier. (d) Typical time courses of H evolution in the systems with different cocatalysts. Reprinted with permission from Ref [?]. Copyright 2017 Royal Society of Chemistry.

2.1.2 Core-Shell Catalysts Core-shell NPs are prevalent catalysts because shell coating improves NP stability and dispersibility while reducing core particle reactivity loss during catalytic experiments [?]. Among various shell candidates, carbon shells are of great interest due to their high chemical and thermal stabilities [?], making carbon-coated core-shell particles very appealing for electrochemical applications. Carbon shells are an inherent feature when implementing LAL in organic solvents (Figure 3a) [?] because the laser-generated plasma is powerful enough to decompose organic molecules into carbon clusters that rapidly precipitate and coalesce on the formed inorganic NPs during rapid plasma quenching (Figure 3c) [?]. To date, a large variety of carbon-coated core-shell NPs have been synthesized by LAL, including TaC@C [?], NbC@C [?], HfC@C [?], MoC@C [?], W C@C [?], Au@C [?], and Co C@C [?]. The onion shell can have as many as 28 carbon layers (Figure 3b) [?]. Some LAL-synthesized carbon-coated particles have shown potential as supercapacitor electrode materials for energy storage, achieving a specific capacitance up to 223 F g⁻¹ (Figure 3d) and slight capacitance loss (<6%) after 5000 charge-discharge cycles (Figure 3e) using LAL-TaC@C assembled electrodes [?].

[Figure 3: see original paper] Formation of inorganic@carbon core-shell particles and their catalytic applications. (a, b) Low and high-resolution TEM images of LAL-synthesized inorganic@carbon core-shell particles. (c) Schematic illustration for the formation process of C-coated core/shell NPs. (d) Comparison of the specific capacitance of TaC@C core-shell NSs with other recently reported carbide-derived carbon and TaC nanowires/activated carbon. (e) Cycling performance of TaC@C core-shell NSs. Reprinted with permission from ref [?]. Copyright 2013 Elsevier. Reprinted with permission from ref [?]. Copyright 2016 Elsevier.

2.1.3 Hollow Catalysts Core-shell NPs serve as excellent sacrificial templates for synthesizing hollow catalysts through dissolution methods, where core materials should be susceptible to acids while shell materials resist acid etching. Hollow particles such as ZnS cages have been successfully synthesized using acid-containing solutions for LAL to trigger in situ etching of the Zn core [?]. Selective etching of LAL-synthesized Zn@ZnO core-shell NPs into hollow Zn cores [?] suggests that hollow ZnO should also be accessible by LAL of Zn targets

in acid solutions. Many other metal@oxide core-shell particles (e.g., Fe@FeO [?], FeMn@FeMn O [?], AuFe@FeO [?]) have been developed by LAL, though no efforts have yet been devoted to transforming them into hollow structures through in situ selective etching LAL.

2.1.4 Composite Catalysts To enhance catalyst stability, prevent electron-hole recombination, or reduce anode and cathode catalyst costs, many efforts have focused on decorating catalysts on supports with high specific surface areas, porosities, electrical conductivities, and thermal/mechanical stabilities, such as oxides [?] (e.g., TiO₂, Al₂O₃, SiO₂, CeO₂) and graphene-derivative layered structures [?]. Traditional techniques (e.g., precipitation and impregnation) and emerging methods (e.g., melt infiltration, colloidal synthesis, atomic layer deposition) are widely adopted for supported catalyst synthesis [?]. Compared to these complicated techniques, LAL provides a one-step platform for spontaneous attachment of target-ejected materials to solid support additives in liquids, termed in situ LAL synthesis of supported catalysts, differing from ex situ synthesis achieved by subsequent colloid mixing (Section 3.3). To date, layered structures (e.g., graphene [?] or graphene oxide (GO) [?]) and particle colloids (e.g., Al₂O₃ [?], CeO₂ [?]) have been utilized for in situ construction of supported catalysts. With defined adsorbent colloidal solutions, simply changing the target composition and comparing resultant catalytic differences induced by adsorbate alternation (e.g., Al₂O₃-AgAu, Al₂O₃-Ag) allows flexible and rapid selection of optimal adsorbates [?]. Additionally, benefiting from highly charged surfaces, LAL/LPL-obtained stable NPs easily assemble into supported catalysts by mixing with oppositely charged support colloids or into film catalysts by electrophoretic deposition (EPD) for device development (Section 3.5).

Ligand-Free Surface Chemistry

[Figure 4: see original paper] Surface chemistry and catalytic reactivity comparison between chemically-synthesized ligand-covered counterparts and LAL-synthesized ligand-free Au NPs. (a) Surface chemistry of citrate-covered and LAL-synthesized ligand-free Au NPs. Reprinted with permission from ref [?]. Copyright 2013 Elsevier. (b) Oxygen evolved upon visible light ($\lambda > 380$ nm) illumination of the FeCl₃ suspension (4 mmol L⁻¹, 50 mL) containing the photocatalysts (50 mg) of LAL-Au/BiFeO₃ and Chem-Au/BiFeO₃ NPs, respectively. Reprinted with permission from ref [?]. Copyright 2013 Royal Society of Chemistry. (c) Cyclic voltammograms (CV) of the Au electrodes formed by LAL-Au NPs and chemically synthesized CTAB-Au NPs in 0.1 mol L⁻¹ NaOH recorded at 20 mV s⁻¹ and at a controlled temperature of 20 °C. The inset shows the underpotential deposition of lead in 0.1 mol L⁻¹ NaOH and 1 mmol L⁻¹ Pb(NO₃)₂ for a LAL-Au NPs-based electrode under the same conditions. Reprinted with permission from ref [?]. Copyright 2015 American Chemical Society.

Most chemically-synthesized particles are covered by ligands [?] (Figure 4a, left) or stabilizers that to some extent change the intrinsic activity of as-prepared

catalysts, sometimes even causing catalytic deactivation [?]. Regarding freedom from surface-impurity influence, LAL-synthesized ligand-free particles [?] (Figure 4a, right) are anticipated to be excellent reference materials for both theoretical studies on catalytic reaction kinetics and experimental enhancement of catalytic reactivities. Findings reported so far have indeed confirmed these hypotheses. For theoretical modeling, strong support comes from the higher fitting rate (70% fitting [?]) of LAL-synthesized Au NPs to the Langmuir-Hinshelwood model based on 4-nitrophenol reduction, compared to chemically-synthesized polyelectrolyte-brush-covered Au NPs (30% fitting [?]). For experimental verification, strong support comes from the remarkably higher reaction rate constant of LAL-synthesized AuNPs ($1.40 \times 10^{-2} \text{ s}^{-1} \text{ m}^{-2}$) over Chem-AuNPs ($2.25 \times 10^{-2} \text{ s}^{-1} \text{ m}^{-2}$) tested as adsorbants on CeO₂ adsorbent supports for 4-nitrophenol reduction [?]. Moreover, Li et al. demonstrated that the photocatalytic activity of LAL-synthesized Au NPs is 1.5 times that of chemically-synthesized Au NPs (Figure 4c) when assembling equal amounts (1.0 wt%) on BiFeO₃ nanowires for water oxidation [?]. Hebié et al. showed that the 2nd cyclic voltammogram (CV) cycle of electrodes assembled from LAL-Au NPs for glucose electrooxidation equals the 10th cycle of electrodes prepared from cetyltrimethylammonium bromide (CTAB)-Au NPs (Figure 4d), thus proving higher electrochemical activity of LAL-Au NPs over chemically-synthesized CTAB-Au NPs [?]. Hence, LAL-synthesized ligand-free metallic catalysts with more active sites are excellent substitutes for ligand-covered catalysts to further promote catalytic performance.

Surface Charge

Zeta potential (-potential) is often used to identify colloidal stability. Generally, when measured zeta potential is above +30 mV or below -30 mV, colloids are stable because repulsive forces among charged NPs are strong enough to maintain dispersion [?]. Table 1 lists zeta potentials of various NPs obtained by LAL or LPL, including Au [?], Ag [?], Cu [?], Mg [?], Pd [?], Ge [?], TiO₂ [?], ZrO₂ [?], and Au@SiO₂ [?]. Synthesis conditions and particle sizes are included to help researchers understand how these colloids are synthesized and their physical states. Most metallic particles synthesized in water are negatively charged. Sylvestre et al. confirmed that M-O and M-OH bindings on particle surfaces induce surface charges that stabilize Au NPs [?]. By measuring zeta potential of LAL-synthesized ZnO NPs with pH adjusted by HCl and NaOH, He et al. revealed that surface states are pH-dependent, with MOH appearing at low pH and M-O forming at high pH [?]. Besides acids and alkalis, ionic buffers can also adjust NP surface charge strength, with Barcikowski's group conducting extensive work in this area [?, ?]. They found that zeta potential of LAL-synthesized particles depends on ionic strength [?] (1-10 mM) and ion type [?] ($\text{F}^{-} < \text{SO}_4^{2-} < \text{Cl}^{-} < \text{NO}_3^{-} < \text{I}^{-} < \text{Br}^{-} < \text{SCN}^{-}$), concluding that ion adsorption plays an important role in stabilizing LAL-synthesized colloids [?]. Detailed effects of ions and pH environments on colloidal nanoparticles are reviewed by Pfeiffer et al. [?]. To obtain positively charged metal particles, cationic surfac-

tant CTAB is an effective additive, where CTA ions first neutralize negatively charged particles and then gradually attach to particle surfaces to form double-layer coatings, resulting in stable particles [?]. Regardless of whether colloids are negatively or positively charged, they are long-term stable for direct use or mixing with oppositely charged supports to form supported composite catalysts (Section 3.3), or assembling into film catalysts by EPD (Section 3.5).

Of great significance, surface charges eliminate ligand requirements like wet chemical synthesis methods, enabling one-step convenient synthesis of NP catalysts. These surface charges also make synthesized NPs “naked” enough to expose more active sites to reactants for sufficient reactions, explaining the higher activities of LAL-synthesized catalysts over chemically-synthesized counterparts shown in Section 2.2.

Zeta potential and particle size of LAL/LPL-synthesized NPs under different synthesis conditions.

Method	Material	Zeta Potential	Particle Size	Synthesis Conditions (targets, laser properties, ablation period, liquids)
LAL	Ag, Cu, Mg	-40 mV	Majority <10 nm	Bulk targets; Ti:sapphire (<10 ps, 1030 nm, 200 kHz, 250 J/pulse); 30 s ablation; 50 mL acetone
LAL	Au	-30 mV	20-80 nm	Nd:YAG (10 ns, 1064 nm, 10 Hz, 90 mJ/pulse); 20 min ablation; 20 mL water
LAL	Pd	-49 mV	9-12 nm	Nd:YAG (8 ns, 1064 nm, 10 kHz, 385 J/pulse); 3 min ablation; 30 mL water
LAL	Au (in water)	-24 to -47 mV	5-40 nm	Gold rod; Ti:sapphire (120 fs, 800 nm, 1 kHz, 0.2 mJ/pulse); 20 min ablation; 3 mL deionized water, or NaCl, KCl, NaNO ₃ , HCl (0.1 N), NaOH (0.1 N)
LAL	Au (with CTAB)	+32 to +40 mV	-	Gold disk; Ti:sapphire (100 fs, 800 nm, 1 kHz, 300 J/pulse); 20 min ablation; 2 mL CTAB aqueous solution or pure deionized water
LAL	Ge	0 to -81 mV	3.4 nm	Ge target; Nd:YAG (9.8 ps, 1064 nm, 100 kHz, 126 J/pulse); 3 min ablation; Milli-Q water, sodium phosphate, sodium carbonate, sodium hydroxide
LAL	TiO ₂	-83 mV	7-8 nm	Ti target; Nd:YAG (10 ns, 1064 nm, 100 mJ/pulse); 5 min ablation; 15 mL deionized water
LAL	ZrO ₂	-45 mV	~23 nm	Zr plate; Nd:YAG (8 ns, 1064 nm, 10 Hz, 120 mJ/pulse); 20 min ablation; 20 mL deionized water

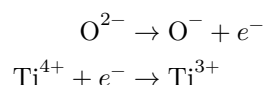
Method	Material	Zeta Potential	Particle Size	Synthesis Conditions (targets, laser properties, ablation period, liquids)
LAL	ZnO	-45 to +30 mV	15-26 nm	Zn plate; Nd:YAG (7 ns, 355 nm, 10 Hz, 100 mJ/pulse); 60 min ablation; HCl (pH 5.36) and NaOH (pH 11.98)
LPL	Au@SnO	-38 mV	16±4 nm	Au target; Nd:YAG (10 ns, 1064 nm, 10 Hz, 60 mJ/pulse); 10 min ablation; 10 mL SnCl ₄ aqueous solution (0.1 M)
LPL	TiO ₂ (anatase)	-37 to -65 mV	12-30 nm	1.5 mg/3.0 mL Au flakes (0.1-0.2 μm); Nd:YAG (6 ns, 1064/532 nm, 10 Hz, 40-100 mJ/pulse); 60 min irradiation; Air, Ar, or O ₂ atmosphere
LPL	TiO ₂ (rutile)	-50 mV	6±3 nm	10 mg/mL anatase-TiO ₂ powder; Nd:YAG (6 ns, 1064 nm, 10 Hz); 60 min irradiation; acetone
LPL	TiO ₂	-59 mV	30 nm	10 mg/mL rutile TiO ₂ powder; Nd:YAG (6 ns, 10 Hz, ~1 J/(pulse · cm ²)); 10 min; deionized water

Unsaturated-Coordination and Oxygen Vacancy Introduction

Metal-oxide semiconductor nanomaterials are excellent photocatalyst candidates [?], with applicability depending on their bandgap and surface defects. Surface oxygen defects behave like unpaired electrons. The extra electrons in vacancies act as donor-like states, creating an accumulation layer in the near-surface region that may cause downward band bending, band flattening, or even upward band bending [?]. Surface-defect-induced bandgap bending also affects light absorption efficiency and influences photocatalytic activity [?] as well as adsorption/desorption of reactant or product molecules [?]. LAL and LPL have proven adept at one-step synthesis of defect-rich, especially oxygen-vacancy-rich oxides (e.g., TiO₂ [?, ?, ?], SnO₂ [?], $x < 2$) that can be used as dopants to develop doped catalysts (e.g., (Ge, Si, Mn, Sn, or Ti)-doped -Fe₂O₃ [?], Section 3.2) or allow in situ reduction of metal ions to develop supported catalysts (e.g., Ag-TiO₂ [?], SnO₂-rGO [?] (reduced graphene oxide), Section 3.3). This section uses TiO₂ as a representative example to show how oxygen vacancies are introduced by LAL/LPL.

Since the Ti/O ratio is 2 for stoichiometric TiO₂, there will be 6 oxygen vacancies in 10 TiO₂ molecules when the atomic Ti/O ratio is 1:1.4 [?]. Generally, oxygen vacancy presence is accompanied by Ti³⁺. For convenience, researchers often use Ti³⁺ concentrations to indirectly characterize oxygen vacancy density. Both X-ray photoelectron spectroscopy (XPS) and electron paramagnetic resonance (EPR) have confirmed Ti³⁺ presence in LPL-prepared TiO₂ colloids [?]. XPS shows that binding energy peaks at 458.9 and 464.7 eV for Ti (2p_{3/2} and 2p_{1/2} core levels) in pristine TiO₂ shift to 458.2 and 462.5 eV after laser irradiation,

fitting well with $\text{Ti}^{3+} 2p_{3/2}$ and $2p_{1/2}$ core levels. Additionally, Ti^{3+} induces an apparent EPR signal, while no signal is observed for pristine TiO_2 . During LPL, high-energy lasers (e.g., $h\nu = 3.49$ eV) trigger electronic transitions between TiO_2 conduction and valence bands ($\text{Ti} 3d$ and $\text{O} 2p$ states, respectively). O atoms donate electrons while Ti^{4+} accepts electrons to form Ti^{3+} , following the reactions shown below [?]. After O atoms are peeled from the TiO_2 NP surface, oxygen vacancies form:



By calculating the ratio of Ti^{3+} peak areas to overall Ti^{3+} and Ti^{4+} peak areas in XPS spectra, Ti^{3+} content can be roughly estimated. The highest $\text{Ti}^{3+}/(\text{Ti}^{3+} + \text{Ti}^{4+})$ atomic ratio is 49%, obtained by LPL of rutile TiO_2 powder in deionized water (10 mg/mL) using a ns Nd:YAG laser (6 ns, 355 nm, 10 Hz, ~ 1 J/(pulse \cdot cm 2)) for 10 min [?]. For LAL, the Ti^{3+} formation mechanism differs. The Ti^{3+} percentage in ($\text{TiO}_2:\text{Ti}^{3+}$) products is laser-energy dependent, with a maximum value of 45.45% [?]. The authors proposed that plasma-related thermodynamic states and rapid quenching processes play critical roles in forming TiO_2 with different Ti^{3+} ratios. Specifically, increasing laser energy creates a relatively higher thermodynamic state during LAL, producing more TiO_2 NPs that become frozen due to rapid plasma plume quenching. Further increasing laser energy extends quenching time, increasing transition opportunities from the metastable TiO_2 state to stable TiO_2 state. The large number of Ti^{3+} and oxygen vacancies in LAL/LPL-obtained TiO_2 NPs enhances photocatalytic performance toward organic molecule degradation (Section 4.1) and hydrogen generation through water splitting (Section 4.2).

Downstream Extension using LAL-Synthesized Colloids

To enrich achievable catalyst diversity, enormous efforts have focused on upgrading LAL/LPL-synthesized NPs into highly advanced catalysts such as ternary oxides, doped catalysts, supported catalysts, nanoparticle-polymer composites, and film catalysts, in combination with various techniques including hydrothermal treatment, colloidal solution mixing, polymerization, and EPD. This section introduces advances in these complex catalysts using LAL/LPL-synthesized NPs as building blocks. Beyond the advanced catalysts presented below, LAL-synthesized colloids can also be constructed into core-shell-NP-supported catalysts (e.g., Fe@C/Pd construction from LAL-obtained Fe@C colloids for m-dichlorobenzene degradation [?]) and capsule-like catalysts (e.g., Au-encapsulated ZnO nanospheres for selective gas sensing [?]).

Ternary Oxide

Ternary oxides, also known as binary metal oxides, contain at least one transition metal ion and one or more electrochemically active/inactive ions, possessing synergistic effects of their constituent oxides for catalytic applications such as supercapacitors [?] and Li-ion batteries [?]. Ternary oxide synthesis is feasible through thermal treatment utilizing high temperature and pressure to dissolve materials and recrystallize products, also applicable to LAL-obtained colloids. Typically, a solution containing active oxide precursors enabling chemical reactions during thermal treatment must be prepared in advance. Two options exist for precursor solution preparation. One is successive LAL of different targets in the same solution. For example, to synthesize Zn GeO NPs, LAL can first be implemented on a Zn target in water. After LAL, the Zn target is replaced by a Ge target while keeping the fresh colloid in the chamber. After LAL, the solution contains both highly active Zn and Ge precursors [?]. The other option is mixing precursor colloids obtained by separate LAL of each target, followed by hydrothermal treatment. This method is more favorable than successive LAL because (1) precursor colloids are easy to control and characterize, and (2) weight ratios between precursor colloids can be flexibly and accurately adjusted.

In 2012, Tian et al. first reported successful synthesis of zinc stannate using LAL-obtained ZnO (OH) and SnO colloidal precursors, manipulating their phase and morphology (e.g., cube-like Zn SnO and urchin-like ZnSnO) by adding different ammonia concentrations (Figure 5a-e) [?]. These ternary oxide photocatalysts displayed good photocatalytic decomposition performance toward methyl orange (MO) and 2,5-dichlorophenol (2,5-DCP), as shown in Figure 5f-g. Inspired by this work, various ternary oxides have been developed by hydrothermal treatment of LAL-synthesized colloid precursors, including Pb-SnO [?], Zn GeO [?], NiCo O [?], Zn SnO [?], ZnFe O [?, ?], NiFe O [?], ZnMnO [?], Fe GeO [?], AgVO [?], BiOCl [?], Bi WO [?], and BiVO [?]. Hydrothermal treatment also allows precursors to react with particle additives to form ternary-oxide-containing composites, enriching product functions. For example, introducing magnetic-field-responsive Fe O @C into LAL-induced Zn and Sn colloidal precursors enables formation of chestnut-like Fe O @C@ZnSnO catalysts (Figure 5h) after hydrothermal treatment, which can be recycled after photocatalytic reactions using an external magnetic field (Figure 5i-j) [?].

[Figure 5: see original paper] Ternary oxide synthesis. (a) Preparation route for synthesizing zinc stannate nanostructures by LAL, colloids mixing and hydrothermal treatment. (b-e) SEM/TEM images and XRD of as-synthesized zinc stannate nanostructures with different amounts of ammonia added: (a, c) 0 mol/L and (b,d) 3.0 mol/L. (f-g) Photocatalysis decomposition of MO and 2,5-DCP, respectively. (h) TEM image and EDX mapping of a single Fe O @C@ZnSnO core-shell particle. (i) Magnetization hysteresis loops of Fe O, Fe O @C, and Fe O @C@ZnSnO measured at room temperature. (j) Cycle evaluation of the photocatalytic removal of 2,5-DCP over the core-shell Fe O @C@ZnSnO particles. Reprinted with permission from ref [?]. Copyright

2012, ref [?]. Copyright 2014 Royal Society of Chemistry.

Doped Catalysts

Doping catalysts with elements (e.g., Si, Ge, Sn, Ti, Nb, Cr, Zn) to modify optical and electrical properties is a widely adopted strategy for performance enhancement, especially attractive for potential commercial catalysts with low cost, abundance, nontoxicity, and stability, such as hematite ($\alpha\text{-Fe}_2\text{O}_3$) [?]. After several years of investigation, LAL-synthesized precursor colloids have proven appropriate as dopants for doped-catalyst development [?, ?]. Liang's group pioneered this field, successfully doping Ge, Si, Mn, Sn, and Ti elements into $\alpha\text{-Fe}_2\text{O}_3$ by hydrothermal treatment of FeCl_3 ions and LAL-synthesized colloids following the mechanism shown in Figure 6a [?]. First, $\alpha\text{-Fe}_2\text{O}_3$ nuclei form upon hydrothermal treatment from FeOOH precursors. Simultaneously, H^+ ions released in solution dissolve LAL-obtained $\text{MO}(\text{OH})_n$ -like clusters ($\text{M} = \text{Ge}, \text{Si}, \text{Mn}, \text{Sn}, \text{Ti}$), generating stable M^{n+} ions (e.g., $\text{Ge}^{4+}, \text{Si}^{4+}, \text{Mn}^{2+}/\text{Mn}^{3+}, \text{Sn}^{4+}, \text{Ti}^{4+}$). These ions participate in $\alpha\text{-Fe}_2\text{O}_3$ NP growth, leading to doped $\alpha\text{-Fe}_2\text{O}_3$ NPs with dopant-determinant morphologies (Figure 6a). Besides composition, dopant concentration also influences as-prepared $\alpha\text{-Fe}_2\text{O}_3$ nanomaterial morphology. For example, 2% Ge-doped $\alpha\text{-Fe}_2\text{O}_3$ forms circular nanosheets (~ 250 nm diameter, ~ 10 nm thickness), while 5% Ge-doped $\alpha\text{-Fe}_2\text{O}_3$ forms hexagonal nanosheets (~ 200 nm aspect size, ~ 10 nm thickness), both differing from undoped hematite $\alpha\text{-Fe}_2\text{O}_3$ cubes and parallelepipeds (Figure 6b-d) [?]. Notably, dopants are not always randomly distributed in $\alpha\text{-Fe}_2\text{O}_3$. Under optimized conditions, dopants (e.g., Ge) can distribute in the hematite lattice in an ordered manner to form superlattice structures [?]. As expected, Ge-doped hematite $\alpha\text{-Fe}_2\text{O}_3$ shows better photoelectrochemical (PEC) performance than undoped hematite, indicated by maximal photocurrent density at different applied potentials.

[Figure 6: see original paper] Doped catalysts synthesis and their catalytic performance. (a) Schematic of the doping process and resulting doped-hematite nanocrystals. Reprinted with permission from ref [?]. Copyright 2012 American Chemical Society. (b-d) Typical SEM images of undoped, 2% Ge-doped, and 5% Ge-doped $\alpha\text{-Fe}_2\text{O}_3$. Reprinted with permission from ref [?]. Copyright 2013 Elsevier. (e-f) Mott-Schottky plots and UV-vis optical absorption spectra of undoped $\alpha\text{-Fe}_2\text{O}_3$ nanorod arrays and Ge-doped $\alpha\text{-Fe}_2\text{O}_3$ nanosheet arrays with annealing temperature of 550°C . Inset shows high magnification SEM image of Ge-doped $\alpha\text{-Fe}_2\text{O}_3$ nanosheet arrays. Reprinted with permission from ref [?]. Copyright 2014 Elsevier.

Solution-drying of colloids to prepare hematite photoanodes often results in disordered stacking of doped nanocrystals. The spatial gap between photoanode materials and underlying conductive substrates generally creates large interface impedance, seriously hindering carrier collection and transport. One solution involves constructing a direct path, such as an array of single-crystal nanostructures on the conductive substrate, to facilitate electron transport to the substrate and photogenerated holes to the catalyst-electrolyte interface. This

raises the question of how to assemble hierarchical nanostructure anodes using LAL-obtained precursor colloids with hydrothermal treatment assistance. As mentioned above, FeOOH serves as γ -Fe₂O₃ precursors [?]. It is reasonable to construct FeOOH-structure films on conductive substrates (e.g., fluorine-doped tin oxide-coated glasses), then immerse these films in LAL-obtained colloidal precursor solutions followed by hydrothermal treatment to construct hematite nanostructure array photoanodes [?]. Liu et al. reported that Ge-doped γ -Fe₂O₃ nanosheet arrays prepared by this method have higher carrier density (Figure 6e) and absorption efficiency (Figure 6f) than undoped γ -Fe₂O₃ nanorod arrays, showing remarkable photocurrent density of 1.4 mA cm⁻² at 1.23 V vs. RHE [?], about tenfold the performance of pure γ -Fe₂O₃ nanorod array anodes [?]. Thus, a new approach for synthesizing doped γ -Fe₂O₃ as either colloids or solid structures has been paved based on LAL-synthesized precursor colloids.

Although no comparative study exists regarding whether LAL-colloids are more favorable than chemically-synthesized counterparts as dopants for catalytic applications, the aforementioned works verify the possibility and demonstrate the potential of using LAL-synthesized precursor colloids as dopants. However, the host catalyst is currently limited to γ -Fe₂O₃; future research should diversify the dopant matrix and host materials, exploiting optimal combinations for different catalytic purposes.

Supported Catalysts

To prevent catalyst agglomeration during reactions, anchoring catalysts on inert supports is often implemented [?]. Charge-driven adsorption based on electrostatic interactions between adsorbent supports and adsorbate (metal or oxide) catalysts is an easy strategy for constructing supported catalysts, widely investigated using innate LAL-synthesized charged particles, such as formation of NYF@TiO₂-Au [?], Au-BiFeO₃ [?], and MWCNT-ZnO [?] for photocatalytic applications, Au/CeO₂ for CO oxidation [?], and Au-TiO₂ for ethanol oxidation [?]. Higher adsorption efficiency is preferable because more catalyst active sites can participate in reactions. Wagener et al. reported that ligand surface coverage plays a dominant role in adsorption efficiency [?]. Completely ligand-free metal NPs and low ligand-coverage NPs allow Freundlich adsorption, while particles covered by citrate ligands with surface coverage 50% are unavailable for NP adsorption on microparticle supports due to electrosteric repulsion induced by ligand shells (Figure 7a-b). As shown in Section 2.3, most LAL-produced metal (e.g., Au) particles are negatively charged, showing high affinity to positively charged supports such as CeO₂ nanotubes. Therefore, almost 100% immobilization of AuNPs on CeO₂ nanotube surfaces (20 mg) was observed within 30 min [?].

To ensure maximal adsorption efficiency, determining the isoelectric point (IEP) of catalyst and support colloidal solutions is indispensable. IEP is the pH value where colloids have no net electrical charge, determined by measuring zeta-potential values while varying colloidal solution pH and NP ionic strength.

Marzun et al. reported a process “window” for sufficient adsorption when considering both ionic strength and pH values, marked in blue in Figure 7c-d [?]. Ionic strength should be controlled within a range ensuring colloidal stability, while pH should lie between the support IEP (IEP-TiO = 6.3) and particle IEP (IEP-Pt = 2.8) to facilitate electrostatic attraction. During adsorption, net charge transfer from NPs to support occurs, causing IEP shift toward the NP IEP (IEP-(Pt-TiO) = 5.0). If electrostatic interaction adjusted by pH and ionic strength is sufficient, the inhibitory effect of NP surface ligands (citrate, polyvinylpyrrolidone (PVP), and lipoic acid (LA)) on adsorption will be weakened or prevented, presenting an avenue to improve adsorption efficiency of ligand-coated NPs. As shown in Table 1, most colloids synthesized by LAL/LPL are sufficiently charged for stabilization. Even when surface charges are in the unstable range of -30 mV to +30 mV, using pH and ionic solutions to strengthen NP surface charge ensures no contamination by ligand additives, ruling out active-site shielding during adsorption.

[Figure 7: see original paper] Adsorption process to construct supported catalysts. (a) Sketch of adsorption process of NPs due to surface coverage. Microparticles covered with ligand-free NPs (left) and unaffected microparticles after mixing with ligand-stabilized NPs (right). Reprinted with permission from ref [?]. Copyright 2012 American Chemical Society. (c) Schematic of Pt-TiO adsorption efficiency controlled by pH and ionic strength. (d) Scheme of nanoparticle adsorption to supports as a function of pH and ionic strength. Reprinted with permission from ref [?]. Copyright 2014 American Chemical Society.

New synthesis paths for supported catalysts have also been paved by in situ reduction of LAL-produced non-stoichiometric oxides (e.g., SnO, TiO) through hydrothermal treatment or aging. For example, Zhang et al. successfully developed Ag-TiO composite catalysts using LAL-obtained defect-rich TiO colloids to reduce Ag ions for photodegradation of pentachlorophenol, substantially enhancing degradation rate from 60% to 98% after 160 min UV irradiation [?]. Ye et al. showed that abundant electrons, surface hydroxyls, and defects in LAL-synthesized SnO colloids can attack oxycarbon atoms of GO, forming stable SnO-rGO composites. Electrodes made from these composites enable non-enzymatic electrochemical sensitive detection (sensitivity of $1.93 \text{ A M}^{-1} \text{ cm}^{-2}$) of trace glucose molecules (detection limit of 13.35 M) [?].

Nanoparticle-Polymer Catalysts

Nanoparticle-polymer composites have gained increasing attention due to combined functions from NPs and polymers. Zhang et al. recently summarized in situ and ex situ laser prototyping approaches for developing various NP-polymer composites and downstream techniques for further functional extension [?]. For catalytic applications, a representative work from Ma's group deserves introduction as it shows the potential of polymer-encapsulated LAL-synthesized particles for multifunctional catalyst development [?]. They grafted thiol-terminated PDEAEMA (SH-PDEAEMA) onto LAL-synthesized Au NPs to develop CO-

switchable and in situ recyclable catalysts [?]. Since Au NPs are naked without ligand coating, surface grafting by SH-PDEAEMA is straightforward, and stable Au-sulfur bonding ensures PDEAEMA-AuNPs colloid stability. The PDEAEMA-AuNPs undergo reversible dispersion upon CO -N purging: CO purging disperses colloids well, while N purging causes aggregation. The performance of PDEAEMA-AuNP and LAL-AuNP catalysts after several reaction cycles for 4-NP reduction shows that PDEAEMA-AuNPs with CO -N purging exhibit much higher catalytic activity than LAL-AuNPs after the first round, attributed to less severe aggregation during sample recycling by centrifugation [?]. Moreover, identical catalytic activity of PDEAEMA-AuNP and LAL-AuNP catalysts in the first round suggests that polymer grafting does not block Au NP active sites. This is crucial from a catalytic application perspective where performance is the main concern. With advancing polymer diversity for NP grafting or encapsulation, polymer functionalization of LAL-synthesized catalysts will offer more choices for flexible manipulation.

Film Catalysts

To develop electrochemical devices, assembling colloids into film catalysts (electrodes) is indispensable. Considering LAL-synthesized colloids are highly charged, direct transformation into film catalysts is easily realized by EPD. Multiple devices have been successfully fabricated along this route, including solar cells [?], neural electrodes [?], biosensor electrodes [?], environmental detector electrodes [?], and electrochromic films [?]. One advantage of using laser-synthesized ligand-free particles for EPD has been revealed by Streich et al. [?]: highly electrophoretically mobile LAL-obtained ligand-free NPs allow controllable barrier-free deposition with linear deposition rate, while ligand-coated NPs only permit limited material deposition [?]. Without other effects in the particle-to-film process chain beyond system factors (e.g., voltage, particle concentration, charge), the highly active sites of LAL-synthesized NPs are well preserved after transformation into film catalysts, which is crucial for sufficient electrode-electrolyte-interface reactions.

If magnetic particles are adopted, magnetophoretic deposition becomes possible. Drop-casting LAL-synthesized NPs (e.g., FeO) onto a substrate (e.g., ITO-coated glass) with a magnet placed below until complete evaporation forms a particle-film electrode [?]. Generally, this yields a coarse electrode surface with uneven NP distribution, and the film is susceptible to mechanical scratching because NPs only physically stack together.

Catalytic Applications

Due to low cost, long lifespan, high power density, good reversibility, and pollution-free operation, electrochemical devices have gained tremendous interest as future sustainable energy suppliers and have been widely investigated using LAL/LPL-obtained electrochemical catalysts for gas sensing [?, ?], biosensing [?, ?], heavy metal ion detection [?], biofuel cells [?], and supercapacitors [?].

When adopting metallic NPs as electrode materials, naked NP surface properties play the dominant role, as introduced in Section 2.2. Therefore, we focus here on the capacities and underlying reasons for excellent photocatalyst performance in photodegradation and water splitting, and present a few LAL/LPL-synthesized catalysts with high commercial potential for fuel-cell applications compared to current commercial products (P25 and Pt/C).

Photodegradation

Organic and heavy metal contaminants cause severe environmental problems threatening natural species and humans, arousing widespread concern for pollutant destruction. As an environmentally friendly and cost-effective method, photodegradation using semiconductor photocatalysts is considered a good choice and has been an active research area for decades [?]. A large variety of photocatalysts have been developed by LAL, LPL, or their combination with downstream techniques (e.g., hydrothermal treatment) for photodegradation of organic molecules (e.g., methylene blue (MB), methyl orange (MO), 2,5-dichlorophenol (2,5-DCP)) or heavy metal ions (e.g., K Cr O), including TiO [?, ?], SnO [?], ZnO [?], -Ag WO [?], ZnSnO [?], Sn O (OH) [?], Fe O @C@ZnSnO [?], Ta O@Ta O [?], TiO /Ti O [?], ZnO/TiO [?], Pt/ZnO [?], MWCNT/ZnO [?], ZnTiO /TiO [?], Au/CeO [?], Sn S [?], ZnS/Zn [?], and titanate nanostructures [?]. Given differences in photocatalyst composition, target degraded molecules, and photocatalyst concentrations, conclusions cannot be drawn regarding which photocatalysts are optimal, especially for LAL-synthesized photocatalysts. The results summarized in Table 2 serve as a reference to guide future investigations from a methodological viewpoint.

Photodegradation of different organic molecules and ions using LAL-synthesized and LPL-obtained nanomaterials.

Method	Materials	Catalytic Experimental Conditions	Performance	Ref
LAL	Sn O (OH)	5 mL of 100 mg L ⁻¹ fresh Sn O (OH) colloid added to 10 mL of 15 ppm MO aqueous solution	97% MO reduction after 25 min irradiation	[?]
LAL	Ta O@Ta O (10-40 nm)	3 mg photocatalyst added to 1.8 ppm (15 mL) MB aqueous solution	92% MB degradation after ~40 min UV irradiation	[?]

Method	Materials	Catalytic Experimental Conditions	Performance	Ref
LPL	TiO ₂ (10-15 nm)	5 mg photocatalyst dispersed in 10 mL aqueous Rh.B solution (10 mg L ⁻¹)	Almost complete Rh.B oxidation after 180 min visible-light irradiation	[?]
LPL	TiO ₂ (a.v. 34 nm)	20 L MB solution (0.05 wt%) added to titanium oxide dispersion (100 g/mL)	90% MB degradation after ~180 min UV irradiation	[?]
LPL	SnO ₂ (a.v. 30 nm)	5 mg SnO ₂ powders added to 30 mL MO solution (25 mg L ⁻¹ , pH = 3.0)	Almost complete MO degradation after 150 min UV irradiation	[?]
LPL	PVP-encapsulated rutile TiO ₂	20 mg TiO ₂ NPs added to methylene blue (1.0×10 ⁻⁴ M, 40 mL)	Almost complete MB reduction after 300 min UV irradiation	[?]
LAL	ZnS/Zn etching nano-cage, ZnS@Zn core-shell NPs (30-50 nm)	2.7 mg ZnS/Zn NPs added to 10 mL 1×10 ⁻² M K ₂ Cr ₂ O ₇ solution	99.9% Cr(IV) reduction using ZnS/Zn nano-cages after 20 min light irradiation	[?]
LAL	SnS (sub-10 nm, porous)	10 mg SnS porous added to 50 mL 1×10 ⁻³ M Cr(VI) solution	99.8% Cr(VI) degradation after 8 min visible light irradiation	[?]

Method	Materials	Catalytic Experimental Conditions	Performance	Ref
LAL	Pt/ZnO (20 nm, Pt 1.1 nm)	10 mg catalyst powders added to 10 M (20 mL) MO solution	90% MO degradation after 40 min UV-light irradiation	[?]
Hydrothermal	ZnSnO (urchin-like, 200 nm)	30 mg L ⁻¹ NPs added to 30 mL MO solution (25 mg L ⁻¹ , pH 7)	98% MO degradation after 90 min and 95% 2,5-DCP degradation after 120 min UV-light irradiation	[?]
Hydrothermal	Hierarchical titanate spheres (150-250 nm)	3 mg titanate spheres added to 30 mL PCP solution (20 mg L ⁻¹ , pH 3) under UV-light	99% PCP degradation in 240 min	[?]
Hydrothermal	FeO @C@ZnSnO (a.v. 600 nm)	50 mg dried FeO @C@ZnSnO powder added to 20 mL 2,5-DCP solution (15 ppm)	87% 2,5-DCP degradation using core-shell FeO @C@ZnSnO NPs	[?]
Hydrothermal	ZnFeO, ZnFeO - rGO	3 mg photocatalysts mixed with 35 mL 12 ppm MB solution + 0.6 mL H ₂ O (30 wt%)	50% MB photodegradation after 300 min using pure ZnFeO NPs; 99.5% using ZnFeO - rGO	[?]

Method	Materials	Catalytic Experimental Conditions	Performance	Ref
Mixing	NYF@TiO - Au (1 wt% Au core@shell micro-spheres, a.v. 500 nm)	10 mg NYF@TiO -Au added to 10 mL MO solution (20 mg L ⁻¹)	96% MO photodegradation after 60 min UV-light irradiation	[?]

Regarding LPL technique competence for photodegradation, TiO photocatalysts serve as the representative because TiO is the most studied photocatalyst due to low cost, high activity, nontoxicity, and long-term chemical/thermal stability. TiO P25 (71 wt% anatase, 29 wt% rutile) enhances reactant adsorption capacity and increases lattice defect and carrier density, serving as a benchmark for evaluating lab-synthesized photocatalysts. Chen et al. compared photocatalytic degradation of rhodamine B using P25, LPL-obtained TiO NPs, and pristine unirradiated TiO NPs (Figure 8a-b) [?]. P25 and pure TiO NPs with 3.3 eV bandgap cannot degrade rhodamine B under visible light, while LPL-obtained TiO NPs show increased photodegradation efficiency. Longer TiO NP irradiation times produce more active catalysts (curves 3-4 in Figure 8b). Surface state analysis revealed that surface lattice disorder, including Ti-H and O-H bonds, induces a 0.4 eV blue-shift of TiO valence band maximum, while Ti³⁺ or oxygen vacancies cause 0.7 eV conduction band position shift (Figure 8a). Therefore, LPL-prepared TiO catalyst bandgap (2.2 eV) is 1.1 eV smaller than unirradiated TiO (3.3 eV), drastically enhancing photocatalytic performance. Ti³⁺ or surface oxygen vacancies create midgap bands near the conduction band (CB) minimum, introducing vacancy-induced bands [?] and enabling enhanced sub-bandgap light absorption [?]. Similarly, large amounts of lattice disorder in TiO NPs may yield midgap states overlapping with or near the valence band (VB) edge, inducing VB edge blue-shift. Electronic reconstruction (0.87 eV band reduction caused by 30.64% Ti³⁺) persists when constructing LAL-synthesized TiO NPs into heterogeneous supported photocatalysts (e.g., TiO -GO) [?]. Yang's group discovered that LPL-induced electronic reconstruction also applies to -Ag WO₃, whose defect density increases by 2.75× and bandgap reduces from 3.22 eV to 2.78 eV after LPL (Figure 8c), greatly enhancing visible-light photodegradation activity and H₂ evolution (Figure 8e) [?]. First-principles calculations theoretically proved bandgap reduction possibility through structural distortion from W atom displacement in [WO₄] clusters (Figure 8d). Increased defect density in semiconductor oxide photocatalysts by LAL or LPL and resultant bandgap reduction promote photocatalytic activities, encouraging extension of LAL/LPL to other oxide photocatalysts.

[Figure 8: see original paper] Photocatalytic activity enhancement due to modi-

fied surface state after LPL. (a) Schematic illustration of electronic density states of TiO₂ before and after laser modification with optical images of counterparts. From left to right: raw TiO₂, TiO₂ -5 min irradiation, TiO₂ -15 min irradiation, TiO₂ -30 min irradiation, TiO₂ -60 min irradiation, and TiO₂ -120 min irradiation. (b) Photocatalytic degradation curves of rhodamine B under green LED irradiation ($\Delta C/C$ vs irradiation time): (1) P25, (2) raw TiO₂, (3) TiO₂ -60, and (4) TiO₂ -120. Adapted with permission from ref [?]. Copyright 2015 American Chemical Society.

Water Splitting/Oxidation

Catalytic splitting of pure water into H₂ and O₂ ($2\text{H}_2\text{O}(l) \rightarrow 2\text{H}_2(g) + \text{O}_2(g)$, $E = -1.23\text{ V}$) through oxygen and hydrogen evolution reactions (OER and HER) by photocatalysts or electrocatalysts is currently a popular global topic because water is almost inexhaustible and hydrogen is considered a next-generation energy carrier for renewable applications [?]. Many material scientists focusing on LAL and LPL have entered this field to reveal advantages of laser-synthesized catalysts. Section 4.1 showed that electronic reconstruction and bandgap reduction of TiO₂ photocatalysts can be induced by modifying surface states (Ti³⁺, oxygen vacancy, surface disorder) using LPL [?]. Therefore, besides photodegradation, hydrogen generation rates for water splitting using LPL-obtained TiO₂ photocatalysts should also be enhanced compared to P25. Compagnini's group recently compared photocatalytic performance of unirradiated and laser-irradiated P25, rutile, and anatase TiO₂, finding that laser-irradiated photocatalysts indeed enhanced hydrogen gas productivity up to $30\text{ mmol g}^{-1}\text{ h}^{-1}$, almost twice that of unirradiated counterparts [?]. Considering the nanosecond laser used for TiO₂ treatment inevitably formed undesirable TiO₂ microspheres, further activity enhancement of LPL-obtained TiO₂ photocatalysts is anticipated by adopting picosecond and femtosecond lasers with negligible melting to minimize catalyst dimensions.

[Figure 9: see original paper] Bandgap reconstruction triggered by LPL. (a) TEM image of LPL-obtained CoO nanoparticles. (b) Hydrogen and oxygen production from CoO nanoparticles (~12 mg) as a function of incident laser power. (c) Ultraviolet-visible diffuse reflectance spectra of CoO nanocrystals and powders. (d) $(F \cdot h\nu)^2$ as a function of photon energy ($h\nu$), where F is the Kubelka-Munk function of diffuse reflectance R . Intercepts of extrapolated straight lines give corresponding direct bandgaps. (e) Mott-Schottky plots for CoO nanocrystals and micropowders from impedance measurements. Flat-band potentials are obtained from extrapolated line intercepts. (f) Band positions of CoO nanocrystals and micropowders according to bandgaps and flat-band potentials from (e). CB, conduction band; VB, valence band. Reprinted with permission from ref [?]. Copyright 2014 Nature Publishing Group.

Ultrasmall catalysts are preferred over large catalysts because they have larger surface-to-volume ratios, exposing more active sites at the same weight and enabling alteration of CB/VB positions. Liao et al. found CoO micropowders

unfeasible for water splitting because the CB edge position (determined from bandgaps and flat-band potentials in Figure 9f) is below the hydrogen-evolution potential [?]. Surprisingly, the CB edge can be elevated above the hydrogen-evolution potential after downsizing CoO micropowders into nanocrystals by LPL (deduced from reflectivity spectra in Figure 9b-c and flat-band potential in Figure 9d). Combined with VB edge positions below the oxygen-evolution potential, this offers water splitting opportunity with solar-to-hydrogen efficiency up to ~5%. Similarly, Blakemore et al. showed possibility of reducing Co micropowders into Co O NPs by long-period (1 h) LAL in water [?]. Such Co O particles are as small as ~2.5 nm without ligand shielding, presenting good electrocatalytic water-oxidation performance with overpotential of 314 mV (measured at 0.5 mA cm⁻²) and high mass activity >10 A m⁻² g⁻¹ at 500 mV overpotential [?]. Overpotential refers to potential above thermodynamic requirement to overcome reaction barriers (given turnover frequency or current density in electrocatalysis) [?].

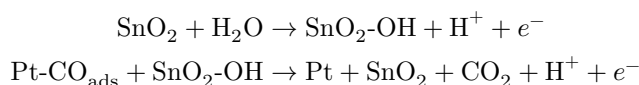
Water oxidation ($2\text{H}_2\text{O}(\text{l}) \rightarrow \text{O}_2(\text{g}) + 4\text{H}^+ + 4\text{e}^-$), a half-reaction of water splitting, is widely investigated because it requires coupling four-electron and four-proton transfer to transform water into hydroxyl radicals ($\text{OH}\cdot$). Catalysts with excellent water-oxidation performance are robust candidates for water splitting. Hu et al. showed that LAL-synthesized PtCo alloy NPs exhibit electrocatalytic activity (mass activity of 0.28 mA/mgPt and specific activity of 1.18 mA/cm²) 2- and 5-times higher than commercial Pt/C (0.09 mA/mgPt and 0.19 mA/cm²) [?]. Novel commercial Pt/C substitutes are anticipated from LAL-synthesized Pt alloys. Moreover, Hunter et al. reported one of the lowest overpotential values (260 mV at 10 mA cm⁻²) for water oxidation using LAL-obtained [Ni-Fe]-layered double hydroxides (LDHs) $\text{Ni}_x\text{Fe}_{1-x}(\text{OH})_2 \cdot n\text{H}_2\text{O}$ [?]. These works demonstrate that LAL and LPL oxide, alloy, and hydroxide products are excellent water splitting catalysts.

Direct Methanol Fuel Cells

[Figure 10: see original paper] Direct methanol fuel cell assembled using LAL-obtained NPs. (a) Schematic illustration for Pt/rGO NCs formation. (b) Mass activities of Pt/rGO and commercial Pt/C catalysts measured in alkaline (0.5 M KOH + 0.5 M CH₃OH) and acidic media (0.5 M H₂SO₄ + 0.5 M CH₃OH) initially, after CA test, and subsequent 1000 cycles. (c) Illustration for synthesis of Pt/SnO₂/rGO hybrid ternary nanocomposites. (d-g) TEM images of reacted suspension colloids at different reaction intervals. Adapted with permission from ref [?]. Copyright 2016 American Chemical Society. (h) HAADF-STEM images of prepared Pt/SnO₂/rGO nanocomposites. (i) CV curves of GC electrodes modified with prepared catalysts measured at 50 mV s⁻¹. (j-k) Mass activities and normalized peak current densities at different cycle numbers for prepared catalysts. Reprinted with permission from ref [?]. Copyright 2016 Elsevier.

Miniaturized fuel cells have been a research hotspot for years to meet increasing demand for portable electronic devices. Direct methanol fuel cells (DMFCs)

based on methanol oxidation to water and carbon dioxide are attractive power sources due to simple structure, high power density, high energy conversion efficiency, and low operation temperature [?]. As core DMFC components, anode electrocatalysts are crucial, with Pt-based materials widely exploited and commercial Pt/C composites serving as performance benchmarks. Wu designed Pt/reduced-graphene-oxide (rGO) nanocomposite electrodes showing superior electrocatalytic activity over commercial Pt/C [?]. LAL-obtained MnO colloids easily dissolved in acid solutions serve as sacrificial templates for in situ reduction of PtCl₂ into Pt NPs (Figure 10d-g). Pt/rGO catalysts have larger electrochemical surface area than Pt/C (1013.4 cm² mg⁻¹ vs 826.9 cm² mg⁻¹, calculated from CV hydrogen adsorption region), higher mass activity (333.3 mA mg⁻¹ vs 153.3 mA mg⁻¹ in acidic media; 552.5 mA mg⁻¹ vs 301.7 mA mg⁻¹ in alkaline media), higher poison tolerance (I_f/I_b peak current density ratio: 7.45 vs 4.46), and longer methanol oxidation stability (85.6% vs 62.4% in acidic media; 77.9% vs 61.4% in alkaline media after 1000 cycles) [?]. Recently, they further enhanced electrocatalytic performance using Pt/SnO₂/rGO nanocomposites constructed by photochemical reduction of PtCl₂ adsorbed on SnO₂ particles (Figure 10h) [?]. Very tiny 1-2 nm Pt NPs are uniformly dispersed on rGO nanosheets (Figure 10i). Mass activity reaches 638.3 mA mg⁻¹ in acidic environments, among the best reported DMFCs [?]. Additionally, Pt/SnO₂/rGO catalyst methanol oxidation peak potential is 0.615 V, 0.084 V lower than 0.699 V for Pt/rGO, indicating easier oxygen-reduction reaction (Figure 10j). Pt/SnO₂/rGO also shows higher stability than Pt/rGO, with 72.4% peak current density remaining after 1200 cycles versus 54.5% for Pt/rGO (Figure 10k-l) [?]. Well-dispersed small Pt NPs, smaller solid-state interfacial resistance from graphene's excellent conductivity, and structural integrity from graphene's stability lead to excellent electrocatalytic performance. The higher activity of Pt/SnO₂/rGO over Pt/rGO arises from synergistic effects between Pt and SnO₂, allowing further oxidation of CO-like species during methanol oxidation:



Conclusion and Perspective

In summary, this decade has witnessed rapid progress in applying laser-synthesized nanomaterials for catalytic applications, mainly benefiting from diverse one-step synthesized catalysts (monometallic, bimetallic, core-shell, and defect-rich NPs) and their adaptability as building blocks for complex catalyst development including ternary oxides, doped semiconductors, supported composites, NP-polymer, and film catalysts with aid from other techniques. In particular, one-step synthesis of advanced catalysts (e.g., Au-FeOCl [?], Au-CoFeO [?], Au-SrTiO₃ [?]) under optimal conditions will bring great convenience. Regarding LAL/LPL-synthesized catalyst properties, unique ligand-free

metallic and defect-rich oxide catalysts endow them with more active sites and narrowed bandgaps, respectively, leading to outstanding catalytic activities [?, ?]. Highly surface-charged and ligand-free features facilitate sufficient adsorption (up to ~100%) of nanocatalysts on various adsorbent supports [?], making them excellent candidates for assembling advanced heterogeneous supported catalysts. Some catalysts have reached performance comparable to or exceeding commercial P25 and Pt/C [?, ?], indicating promising future as next-generation commercial catalysts. Another appealing feature is the technique's strength in one-step alloying of transition metals (Fe, Mn, Cu, Co, Ni) with each other or with noble metals (Au, Pt) into cost-effective nanoalloys [?, ?, ?], potentially greatly reducing catalyst synthesis costs.

It is well known that catalyst performance depends on composition, morphology, and size. Many challenges remain for accurately manipulating physical properties (size, morphology) and surface chemistry because controlling plasma generation-quenching processes is difficult. Jendrzej et al. observed atom-scale metallic clusters obtained by LPL, whose catalytic applications are promising [?]. Nevertheless, coalescence and ripening of atom clusters in liquids enlarge their size and deteriorate activity. Therefore, appropriate preservation methods (e.g., freezing) should be exploited to prevent agglomeration before catalytic use. From the reviewed literature, it is clear that most reported catalysts are metal-related, with few metal-free catalysts. Future studies should investigate developing active metal-free catalysts using LAL/LPL.

Acknowledgements

This work was financially supported by the National Basic Research Program of China (2014CB931704), the National Natural Science Foundation of China (NSFC, nos. 11304315, 51401206, 11404338, 51371166, 51571186, 11504375), and the CAS/SAFEA International Partnership Program for Creative Research Teams.

References

- [1] a) L. Mai, X. Tian, X. Xu, L. Chang and L. Xu, *Chem. Rev.* 2014, 114, 11828-11862; b) M. R. Hoffmann, S. T. Martin, W. Choi and D. W. Bahnemann, *Chem. Rev.* 1995, 95, 69-96; c) N. Nitta and G. Yushin, *Part. Part. Syst. Charact.* 2014, 31, 317-336; d) T. Montini, M. Melchionna, M. Monai and P. Fornasiero, *Chem. Rev.* 2016, 116, 5987-6041. [2] C.-J. Jia and F. Schuth, *Phys. Chem. Chem. Phys.* 2011, 13, 2457-2487. [3] Z. Niu and Y. Li, *Chem. Mater.* 2013, 26, 72-83. [4] J. A. Lopez-Sanchez, N. Dimitratos, C. Hammond, G. L. Brett, L. Kesavan, S. White, P. Miedziak, R. Tiruvalam, R. L. Jenkins and A. F. Carley, *Nat. Chem.* 2011, 3, 551-556. [5] a) F. Mafuné, J.-y. Kohno, Y. Takeda, T. Kondow and H. Sawabe, *J. Phys. Chem. B* 2001, 105, 5114-5120; b) A. Fojtik and A. Henglein, *Ber. Bunsenges. Phys. Chem.* 1993, 97, 252-254; c) J. Nedderson, G. Chumanov and T. M. Cotton, *Appl. Spectrosc.* 1993, 47, 1959-

1964; d) J. Liu, C. Liang, Z. Tian, S. Zhang and G. Shao, *Sci. Rep.* 2013, 3, 1741. [6] a) A. V. Kabashin and M. Meunier, *J. Appl. Phys.* 2003, 94, 7941-7943; b) D. Zhang, B. Gökce, C. Notthoff and S. Barcikowski, *Sci. Rep.* 2015, 5, 13661. [7] G. Marzun, J. Nakamura, X. Zhang, S. Barcikowski and P. Wagener, *Appl. Surf. Sci.* 2015, 348, 75-84. [8] S. Scaramuzza, S. Agnoli and V. Amendola, *Phys. Chem. Chem. Phys.* 2015, 17, 10576-10584. [9] Y.-H. Chen and C.-S. Yeh, *Colloids Surf., A* 2002, 197, 133-139. [10] D. Zhang and B. Gökce, *Appl. Surf. Sci.* 2016, 392, 991-1003. [11] D. Zhang, Z. Ma, M. Spasova, A. E. Yelsukova, S. Lu, M. Farle, U. Wiedwald and B. Gökce, *Part. Part. Syst. Charact.* 2017, 34, 1600225. [12] M. Dell' Aglio, R. Gaudiuso, O. De Pascale and A. De Giacomo, *Appl. Surf. Sci.* 2015, 348, 4-9. [13] D. Zhang, B. Gökce, S. Sommer, R. Streubel and S. Barcikowski, *Appl. Surf. Sci.* 2016, 367, 222-230. [14] S. Ibrahimkutti, P. Wagener, A. Menzel, A. Plech and S. Barcikowski, *Appl. Phys. Lett.* 2012, 101, 103104. [15] V. Amendola and M. Meneghetti, *Phys. Chem. Chem. Phys.* 2013, 15, 3027-3046. [16] S. Jendrzey, B. Gökce, V. Amendola and S. Barcikowski, *J. Colloid Interf. Sci.* 2016, 463, 299-307. [17] J. Liu, C. Liang, X. Zhu, Y. Lin, H. Zhang and S. Wu, *Sci. Rep.* 2016, 6, 32631. [18] C. Liang, T. Sasaki, Y. Shimizu and N. Koshizaki, *Chem. Phys. Lett.* 2004, 389, 58-63. [19] a) A. Takami, H. Kurita and S. Koda, *J. Phys. Chem. B* 1999, 103, 1226-1232; b) S. Link, C. Burda, B. Nikoobakht and M. A. El-Sayed, *J. Phys. Chem. B* 2000, 104, 6152-6163. [20] a) C. Liang, S. Wu, E. Dai, Y. Ye, J. Liu, Z. Tian, Y. Cai, X. Zhu and Y. Han, *ChemPhysChem* 2017, DOI: 10.1002/cphc.201601185; b) D. Zhang, M. Lau, S. Lu, S. Barcikowski and B. Gökce, *Sci. Rep.* 2017, 7, 40355; c) H. Wang, N. Koshizaki, L. Li, L. Jia, K. Kawaguchi, X. Li, A. Pyatenko, Z. Swiatkowska-Warkocka, Y. Bando and D. Golberg, *Adv. Mater.* 2011, 23, 1865-1870; d) H. Wang, M. Miyauchi, Y. Ishikawa, A. Pyatenko, N. Koshizaki, Y. Li, L. Li, X. Li, Y. Bando and D. Golberg, *J. Am. Chem. Soc.* 2011, 133, 19102-19109. [21] K. Yamada, K. Miyajima and F. Mafuné, *J. Phys. Chem. C* 2007, 111, 11246-11251. [22] A. Pyatenko, H. Wang, N. Koshizaki and T. Tsuji, *Laser Photonics Rev.* 2013, 7, 596-617. [23] R.-C. Luo, C. Li, X.-W. Du and J. Yang, *Angew. Chem. Int. Ed.* 2015, 54, 4780-4784. [24] X. Chen, D. Zhao, K. Liu, C. Wang, L. Liu, B. Li, Z. Zhang and D. Shen, *ACS Appl. Mater. Interfaces* 2015, 7, 16070-16077. [25] H. J. Jung and M. Y. Choi, *J. Phys. Chem. C* 2014, 118, 14647-14654. [26] H. Zhang, S. Wu, J. Liu, Y. Cai and C. Liang, *Phys. Chem. Chem. Phys.* 2016, 18, 22503-22508. [27] A. Poletti, G. Fracasso, G. Conti, R. Pilot and V. Amendola, *Nanoscale* 2015, 7, 17989-17996. [28] W. Li, X. Ge, H. Zhang, Q. Ding, H. Ding, Y. Zhang, G. Wang, H. Zhang and H. Zhao, *Inorg. Chem. Front.* 2016, 3, 663-670. [29] C. A. Schaumberg, M. Wollgarten and K. Rademann, *J. Phys. Chem. A* 2014, 118, 8329-8337. [30] H. Zeng, X. W. Du, S. C. Singh, S. A. Kulinich, S. Yang, J. He and W. Cai, *Adv. Funct. Mater.* 2012, 22, 1333-1353. [31] D. Wang and Y. Li, *Adv. Mater.* 2011, 23, 1044-1060. [32] R. Ferrando, J. Jellinek and R. L. Johnston, *Chem. Rev.* 2008, 108, 845-910. [33] G. Marzun, A. Levish, V. Mackert, T. Kallio, S. Barcikowski and P. Wagener, *J. Colloid Interf. Sci.* 2017, 489, 57-67. [34] a) S. b. Besner and M. Meunier, *J. Phys. Chem. C* 2010, 114, 10403-10409; b) J. Zhang, J. Worley, S. Dénomée,

C. Kingston, Z. J. Jakubek, Y. Deslandes, M. Post, B. Simard, N. Braid and G. A. Botton, *J. Phys. Chem. B* 2003, 107, 6920-6923. [35] P. Wagener, J. Jakobi, C. Rehbock, V. S. K. Chakravadhanula, C. Thede, U. Wiedwald, M. Bartsch, L. Kienle and S. Barcikowski, *Sci. Rep.* 2016, 6, 23352. [36] K. D. Malviya and K. Chattopadhyay, *J. Phys. Chem. C* 2016, 120, 27699-27706. [37] K. D. Malviya and K. Chattopadhyay, *J. Phys. Chem. C* 2014, 118, 13228-13237. [38] A. Neumeister, J. Jakobi, C. Rehbock, J. Moysig and S. Barcikowski, *Phys. Chem. Chem. Phys.* 2014, 16, 23671-23678. [39] J. Zhang, G. Chen, D. Guay, M. Chaker and D. Ma, *Nanoscale* 2014, 6, 795-799. [40] D. N. Oko, S. Garbarino, J. Zhang, Z. Xu, M. Chaker, D. Ma, D. Guay and A. C. Tavares, *Electrochim. Acta* 2015, 159, 174-183. [41] Z. Lin, J. Li, L. Li, L. Yu, W. Li and G. Yang, *J. Mater. Chem. A* 2017, 5, 4555-4560. [42] H. Zhang, C. Liang, J. Liu, Z. Tian and G. Shao, *Carbon* 2013, 55, 108-115. [43] H. Zhang, J. Liu, Z. Tian, Y. Ye, Y. Cai, C. Liang and K. Terabe, *Carbon* 2016, 100, 590-599. [44] R. Ghosh Chaudhuri and S. Paria, *Chem. Rev.* 2011, 112, 2373-2433. [45] D. S. Su, S. Perathoner and G. Centi, *Chem. Rev.* 2013, 113, 5782-5816. [46] S. Yang, W. Cai, H. Zhang, H. Zeng and Y. Lei, *J. Phys. Chem. C* 2011, 115, 13091-13096. [47] R. G. Calzada, K. Bagga, P. Bianchini, V. Chirvony and J. P. Martínez-Pastor, *RSC Adv.* 2015, 5, 50604-50610. [48] D. Wang, H. Zhang, L. Li, M. Chen and X. Liu, *Opt. Mater. Express* 2016, 6, 217-223. [49] a) H. Zeng, W. Cai, P. Liu, X. Xu, H. Zhou, C. Klingshirn and H. Kalt, *ACS Nano* 2008, 2, 1661-1670; b) H. Zeng, P. Liu, W. Cai, S. Yang and X. Xu, *J. Phys. Chem. C* 2008, 112, 19620-19624. [50] V. Amendola, P. Riello and M. Meneghetti, *J. Phys. Chem. C* 2011, 115, 5140-5146. [51] V. Amendola, S. Scaramuzza, F. Carraro and E. Cattaruzza, *J. Colloid Interf. Sci.* 2016, 489, 18-27. [52] P. Munnik, P. E. de Jongh and K. P. de Jong, *Chem. Rev.* 2015, 115, 6687-6718. [53] M. Liu, R. Zhang and W. Chen, *Chem. Rev.* 2014, 114, 5117-5160. [54] R. S. Sai Siddhardha, V. Lakshman Kumar, A. Kaniyoor, V. Sai Muthukumar, S. Ramaprabhu, R. Podila, A. M. Rao and S. S. Ramamurthy, *Spectrochim. Acta, Part A* 2014, 133, 365-371. [55] P. Wang, Y. Ye, D. Liang, H. Sun, J. Liu, Z. Tian and C. Liang, *RSC Adv.* 2016, 6, 55287-55294. [56] R. Singh and R. K. Soni, *J. Nanosci. Nanotechnol.* 2014, 14, 6872-6879. [57] R. Ma, Y.-j. Kim, D. Amaranatha Reddy and T. K. Kim, *Ceram. Int.* 2015, 41, 7844-7852. [58] K. B. Cederquist, B. Liu, M. R. Grima, P. J. Dalack and J. T. Mahorn, *Colloids Surf. B Biointerfaces* 2017, 149, 351-357. [59] S. Li, J. Zhang, M. G. Kibria, Z. Mi, M. Chaker, D. Ma, R. Nechache and F. Rosei, *Chem. Commun.* 2013, 49, 5856-5858. [60] S. Hebié, Y. Holade, K. Maximova, M. Sentis, P. Delaporte, K. B. Kokoh, T. W. Napporn and A. V. Kabashin, *ACS Catal.* 2015, 5, 6489-6496. [61] S. Gu, J. Kaiser, G. Marzun, A. Ott, Y. Lu, M. Ballauff, A. Zacccone, S. Barcikowski and P. Wagener, *Catal. Lett.* 2015, 145, 1105-1112. [62] S. Gu, S. Wunder, Y. Lu, M. Ballauff, R. Fenger, K. Rademann, B. Jaquet and A. Zacccone, *J. Phys. Chem. C* 2014, 118, 18618-18625. [63] J. Zhang, G. Chen, M. Chaker, F. Rosei and D. Ma, *Appl. Catal., B* 2013, 132, 531-538. [64] T. M. Riddick in *Zeta-Meter Operating Manual zm-75*, Zeta-Meter, Inc., New York, 1968. [65] a) H. He, W. Cai, Y. Lin and B. Chen, *Langmuir* 2010, 26, 8925-8932; b) M. A. Sobhan, M. J. Withford and E. M. Goldys, *Langmuir* 2009, 26,

3156-3159; c) D. Werner, S. Hashimoto, T. Tomita, S. Matsuo and Y. Makita, *J. Phys. Chem. C* 2008, 112, 16801-16808; d) J.-P. Sylvestre, S. Poulin, A. V. Kabashin, E. Sacher, M. Meunier and J. H. T. Luong, *J. Phys. Chem. B* 2004, 108, 16864-16869. [66] N. Bärsch, J. Jakobi, S. Weiler and S. Barcikowski, *Nanotechnology* 2009, 20, 445603. [67] a) H. Zhang, C. Liang, J. Liu, Z. Tian, G. Wang and W. Cai, *Langmuir* 2012, 28, 3938-3944; b) T. Tsuji, M. Nakanishi, T. Mizuki, M. Tsuji, T. Doi, T. Yahiro and J. Yamaki, *Appl. Surf. Sci.* 2009, 255, 9626-9629; c) S. S. Pan, W. Lu, Y. H. Zhao, W. Tong, M. Li, L. M. Jin, J. Y. Choi, F. Qi, S. G. Chen, L. F. Fei and S. F. Yu, *ACS Appl. Mater. Interfaces* 2013, 5, 12784-12788. [68] H. Bao, Y. Wang, H. Zhang, Q. Zhao, G. Liu and W. Cai, *J. Colloid Interf. Sci.* 2017, 489, 92-99. [69] C. He, T. Sasaki, H. Usui, Y. Shimizu and N. Koshizaki, *J. Photochem. Photobiol., A* 2007, 191, 66-73. [70] C. Rehbock, V. Merk, L. Gamrad, R. Streubel and S. Barcikowski, *Phys. Chem. Chem. Phys.* 2013, 15, 3057-3067. [71] V. Merk, C. Rehbock, F. Becker, U. Hagemann, H. Nienhaus and S. Barcikowski, *Langmuir* 2014, 30, 4213-4222. [72] C. Pfeiffer, C. Rehbock, D. Hühn, C. Carrillo-Carrion, D. J. de Aberasturi, V. Merk, S. Barcikowski and W. J. Parak, *J. R. Soc. Interface* 2014, 11, 20130931. [73] H. Muto, K. Yamada, K. Miyajima and F. Mafuné, *J. Phys. Chem. C* 2007, 111, 17221-17226. [74] C. Streich, S. Koenen, M. Lelle, K. Peneva and S. Barcikowski, *Appl. Surf. Sci.* 2015, 348, 92-99. [75] a) J. Schneider, M. Matsuoka, M. Takeuchi, J. Zhang, Y. Horiuchi, M. Anpo and D. W. Bahnemann, *Chem. Rev.* 2014, 114, 9919-9986; b) U. Diebold, *Surf. Sci. Rep.* 2003, 48, 53-229. [76] I. Justicia, P. Ordejon, G. Canto, J. L. D. L. M. D. L. Mozos, J. Fraxedas, G. A. Battiston, R. Gerbasi and A. Figueras, *Adv. Mater.* 2002, 14, 1399-1402. [77] Z. Zhang and J. T. Yates, *Chem. Rev.* 2012, 112, 5520-5551. [78] L. Li, L. Yu, Z. Lin and G. Yang, *ACS Appl. Mater. Interfaces* 2016, 8, 22460-22467. [79] a) C. Liang, Y. Shimizu, T. Sasaki and N. Koshizaki, *J. Phys. Chem. B* 2003, 107, 9220-9225; b) Z. Tian, C. Liang, J. Liu, H. Zhang and L. Zhang, *J. Mater. Chem.* 2011, 21, 18242-18247. [80] J. Liu, C. Liang, H. Zhang, Z. Tian and S. Zhang, *J. Phys. Chem. C* 2012, 116, 9347-9353. [81] Y. Ye, P. Wang, E. Dai, J. Liu, Z. Tian, C. Liang and G. Shao, *Phys. Chem. Chem. Phys.* 2014, 16, 8801-8807. [82] L. Li, Z. Deng, J. Xiao and G. Yang, *Nanotechnology* 2015, 26, 255705. [83] Y. Yu, H. J. Jung, M. Je, H. C. Choi and M. Y. Choi, *Chemosphere* 2016, 155, 406-414. [84] Y. Zhang, L. Li, H. Su, W. Huang and X. Dong, *J. Mater. Chem. A* 2015, 3, 12592-12601. [85] M. V. Reddy, G. V. Subba Rao and B. V. R. Chowdari, *Chem. Rev.* 2013, 113, 5364-5457. [86] M. Rui, X. Li, L. Gan, T. Zhai and H. Zeng, *Adv. Funct. Mater.* 2016, DOI: 10.1002/adfm.201600785. [87] Z. Tian, C. Liang, J. Liu, H. Zhang and L. Zhang, *J. Mater. Chem.* 2012, 22, 10978-10984. [88] S. Wu, P. Wang, Y. Cai, D. Liang, Y. Ye, Z. Tian, J. Liu and C. Liang, *RSC Adv.* 2015, 5, 9069-9074. [89] Z. Tian, S. Wu, P. Wang, Y. Cai, D. Liang, Y. Ye, J. Liu and C. Liang, *CrystEngComm* 2015, 17, 3015-3022. [90] D. Liang, S. Wu, P. Wang, Y. Cai, Z. Tian, J. Liu and C. Liang, *RSC Adv.* 2014, 4, 58444-58450. [91] a) Z. Zhou, P. Huo, L. Guo and O. V. Prezhdo, *J. Phys. Chem. C* 2015, 119, 26303-26310; b) S. Kumari, A. P. Singh, C. Tripathi, D. Chauhan, S. Dass, R. Shrivastav, V. Gupta, K. Sreenivas and V. R. Satsangi, *Int. J. Photoenergy*

2007, 2007, 76473. [92] a) J. Liu, C. Liang, G. Xu, Z. Tian, G. Shao and L. Zhang, *Nano Energy* 2013, 2, 328-336; b) J. Liu, C. Liang, H. Zhang, S. Zhang and Z. Tian, *Chem. Commun.* 2011, 47, 8040-8042. [93] J. Liu, Y. Y. Cai, Z. F. Tian, G. S. Ruan, Y. X. Ye, C. H. Liang and G. S. Shao, *Nano Energy* 2014, 9, 282-290. [94] G. Ruan, S. Wu, P. Wang, J. Liu, Y. Cai, Z. Tian, Y. Ye, C. Liang and G. Shao, *RSC Adv.* 2014, 4, 63408-63413. [95] Z. Xu, M. Quintanilla, F. Vetrone, A. O. Govorov, M. Chaker and D. Ma, *Adv. Funct. Mater.* 2015, 25, 2950-2960. [96] T. A. Saleh, M. Gondal and Q. Drmosh, *Nanotechnology* 2010, 21, 495705. [97] W. Dong, S. Reichenberger, S. Chu, P. Weide, H. Ruland, S. Barcikowski, P. Wagener and M. Muhler, *J. Catal.* 2015, 330, 497-506. [98] P. Wagener, A. Schwenke and S. Barcikowski, *Langmuir* 2012, 28, 6132-6140. [99] G. Marzun, C. Streich, S. Jendrzey, S. Barcikowski and P. Wagener, *Langmuir* 2014, 30, 11928-11936. [100] J. Zhang, D. Han, H. Zhang, M. Chaker, Y. Zhao and D. Ma, *Chem. Commun.* 2012, 48, 11510-11512. [101] a) W. Guo and B. Liu, *ACS Appl. Mater. Interfaces* 2012, 4, 7036-7042; b) V. Svrcek, D. Mariotti, T. Nagai, Y. Shibata, I. Turkevych and M. Kondo, *J. Phys. Chem. C* 2011, 115, 5084-5093. [102] S. D. Angelov, S. Koenen, J. Jakobi, H. E. Heissler, M. Alam, K. Schwabe, S. Barcikowski and J. K. Krauss, *J. Nanobiotechnol.* 2016, 14, 3. [103] P. Kalita, J. Singh, M. K. Singh, P. R. Solanki, G. Sumana and B. Malhotra, *Appl. Phys. Lett.* 2012, 100, 093702. [104] X. Xu, G. Duan, Y. Li, G. Liu, J. Wang, H. Zhang, Z. Dai and W. Cai, *ACS Appl. Mater. Interfaces* 2013, 6, 65-71. [105] S. Wang, K. Dou, Y. Zou, Y. Dong, J. Li, D. Ju and H. Zeng, *J. Colloid Interf. Sci.* 2017, 489, 85-91. [106] E. Pizzolato, S. Scaramuzza, F. Carraro, A. Sartori, S. Agnoli, V. Amendola, M. Bonchio and A. Sartorel, *J. Energy Chem.* 2016, 25, 246-250. [107] a) Z. Li, C. Dong, J. Yang, S. Qiao and X. Du, *J. Mater. Chem. A* 2016, 4, 2699-2704; b) J. Xiao, P. Liu, Y. Liang, H. B. Li and G. W. Yang, *J. Appl. Phys.* 2013, 114, 073513. [108] H. Zhang, J. Liu, Y. Ye, Z. Tian and C. Liang, *Phys. Chem. Chem. Phys.* 2013, 15, 5684-5690. [109] a) M. Zimbone, M. A. Buccheri, G. Cacciato, R. Sanz, G. Rappazzo, S. Boninelli, R. Reitano, L. Romano, V. Privitera and M. G. Grimaldi, *Appl. Catal., B* 2015, 165, 487-494; b) M. A. Pugachevskii, *Nanosci. Nanotechnol. Lett.* 2014, 6, 519-523; c) M. Zimbone, G. Cacciato, M. A. Buccheri, R. Sanz, N. Piluso, R. Reitano, F. La Via, M. G. Grimaldi and V. Privitera, *Mat. Sci. Semicon. Proc.* 2016, 42, 28-31; d) P. Liu, W. Cai, M. Fang, Z. Li, H. Zeng, J. Hu, X. Luo and W. Jing, *Nanotechnology* 2009, 20, 285707. [110] Z. Lin, J. Li, Z. Zheng, J. Yan, P. Liu, C. Wang and G. Yang, *ACS Nano* 2015, 9, 7256-7265. [111] J. Xiao, Q. L. Wu, P. Liu, Y. Liang, H. B. Li, M. M. Wu and G. W. Yang, *Nanotechnology* 2014, 25, 135702. [112] Q. Li, C. Liang, Z. Tian, J. Zhang, H. Zhang and W. Cai, *CrystEngComm* 2012, 14, 3236-3240. [113] M. A. Gondal, A. M. Ilyas and U. Baig, *Ceram. Inter.* 2016, 42, 13151-13160. [114] Y. Cai, Y. Ye, Z. Tian, J. Liu, Y. Liu and C. Liang, *Phys. Chem. Chem. Phys.* 2013, 15, 20203-20209. [115] Z. Wang, Z. Wang, D. Wang and M. Chen, *RSC Adv.* 2016, 6, 12286-12289. [116] H. Zhang, C. Liang, Z. Tian, J. Liu and W. Cai, *CrystEngComm* 2011, 13, 2006-2011. [117] F. Zuo, L. Wang, T. Wu, Z. Zhang, D. Borchardt and P. Feng, *J. Am. Chem. Soc.* 2010, 132, 11856-11857. [118] J. Ran, J. Zhang, J. Yu, M. Jaroniec and S. Z. Qiao, *Chem.*

Soc. Rev. 2014, 43, 7787-7812. [119] S. Filice, G. Compagnini, R. Fiorenza, S. Scirè, L. D' Urso, M. E. Fragalà, P. Russo, E. Fazio and S. Scalese, J. Colloid Interf. Sci. 2017, 489, 131-137. [120] L. Liao, Q. Zhang, Z. Su, Z. Zhao, Y. Wang, Y. Li, X. Lu, D. Wei, G. Feng and Q. Yu, Nat. Nanotechnol. 2014, 9, 69-73. [121] J. D. Blakemore, H. B. Gray, J. R. Winkler and A. M. Müller, ACS Catal. 2013, 3, 2497-2500. [122] B. M. Hunter, H. B. Gray and A. M. Müller, Chem. Rev. 2016, 116, 14120-14136. [123] S. Hu, M. Tian, E. L. Ribeiro, G. Duscher and D. Mukherjee, J. Power Sources 2016, 306, 413-423. [124] B. M. Hunter, J. D. Blakemore, M. Deimund, H. B. Gray, J. R. Winkler and A. M. Müller, J. Am. Chem. Soc. 2014, 136, 13118-13121. [125] S. Wu, J. Liu, Z. Tian, Y. Cai, Y. Ye, Q. Yuan and C. Liang, ACS Appl. Mater. Interfaces 2015, 7, 22935-22940. [126] S. Wu, J. Liu, D. Liang, H. Sun, Y. Ye, Z. Tian and C. Liang, Nano Energy 2016, 26, 699-707. [127] D. S. Falcão, V. B. Oliveira, C. M. Rangel and A. M. F. R. Pinto, Renew. Sust. Energy Rev. 2014, 34, 58-70. [128] H. Huang and X. Wang, J. Mater. Chem. A 2014, 2, 6266-6291. [129] Y. Wang, H. Zhang, Y. Zhu, Z. Dai, H. Bao, Y. Wei and W. Cai, Adv. Mater. Interfaces 2016, DOI: 10.1002/admi.201500801. [130] J. L. Guo, Y. D. Chiou, W. I. Liang, H. J. Liu, Y. J. Chen, W. C. Kuo, C. Y. Tsai, K. A. Tsai, H. H. Kuo and W. F. Hsieh, Adv. Mater. 2013, 25, 2040-2044.

Entry for the Table of Contents (Please choose one layout)

FOCUS REVIEW

This focus review demonstrates the strength of a new technique—laser ablation/processing in liquids—in one-step synthesis of ligand-free catalysts without surfactant additives and its excellence at defect introduction to semiconductor photocatalysts.

Dongshi Zhang, Jun Liu, Pengfei Li, Zhenfei Tian, Changhao Liang*

Page No. -Page No.

Recent Advances in Ligand-Free, Charged and Defect-Rich Catalysts Developed by Laser Ablation and Processing in Liquids

Dr. Dongshi Zhang obtained his Ph.D. from Xi'an Jiaotong University (China) in 2014 and worked in Prof. Stephan Barcikowski's group at the University of Duisburg-Essen (Germany) from 2014 to 2016. Currently, he works in Prof. Changhao Liang's group to further his research. His research interests include laser ablation, laser microfabrication, laser cutting, and their combination with surface chemistry for wettability control and with inorganic chemistry for novel nanomaterial synthesis.

Changhao Liang obtained his Ph.D. from the Institute of Solid State Physics, Chinese Academy of Sciences in 2001. He is currently a full professor in the Laboratory of Nanostructured Materials, Institute of Solid State Physics. His

current research interests lie in laser-material interactions in liquids, nanoionics-based resistive switching devices, and nanomaterials for energy & environmental applications.

Note: Figure translations are in progress. See original paper for figures.

Source: ChinaXiv –Machine translation. Verify with original.